Bifunctional device with high energy storage density and ultralow current analog resistive switching

*Qian Liu, Qiang Xue, Yanbin Wang, Xianhua Wei *, Jianhua Hao **

Q. Liu, Q. Xue,Y. B. Wang, Prof. X. H. Wei

State Key Laboratory of Environment-friendly Energy Materials, Southwest University of Science and Technology, Mianyang 621010, P. R. China

Xianhua Wei, Email: weixianhua@swust.edu.cn

Prof. J. H. Hao

Department of Applied Physics, The Hong Kong Polytechnic University, Hung Hom, Kowloon, Hong Kong, P. R. China

Jianhua Hao, Email: jh.hao@polyu.edu.hk

Keywords: energy storage, resistive switching, bifunction, oxide interface, breakdown strength

Abstract

A bifunctional device capable of simultaneously achieving dielectric energy storage and resistive switching is firstly designed and fabricated based on a conventional metal-insulator-metal (MIM) structure. Typically, Al/TaO_x/Pt structure shows a high breakdown strength up to 5.07 MV cm^{-1} and a relatively high energy density of 27.6 J cm^{-3}. Meanwhile, the leakage current of the MIM structure is as low as sub-nanoampere level and exhibits a typical characteristic of analog switching under the applied voltage of about a dozen volts. The energy density and the switching current in the developed integrated MIM structure are comparable to the corresponding performances in discrete binary oxides capacitors with linear dielectric and oxide-based memristors, respectively. Furthermore, synaptic functions with short-term and long-term plasticities can be realized. Both of the device properties are found to be correlated to the role of AlO_x interfacial layer between Al electrode and the dielectric layer, which provides the possibility of coupling between these two functions co-existed in the MIM structure. The prototypical bifunctional device offers a great prospect for multifunctional energy and neuromorphic applications.

1. Introduction

The memristor was proposed as the fourth fundamental circuit element after resistor, capacitor, and inductor by Chua in 1971.[1] Recently, the new concept device has attracted considerable attention not only due to its potential application in memory with high density integration, but also for its ambition to pass the von Neumann bottleneck and Moore's law era by combining bioinspired and in-memory computing abilities.[2,3] A memristor cell is generally composed of a metal/insulator/metal (MIM) sandwich structure in which the resistance can be switched between high resistance state (HRS) and low resistance state (LRS) reversibly under applied electrical stimulus.[4,5] Considerable efforts have been extended to combine the memristor and other functional units such as the supercapacitor and light-emitting device for multifunctional application.[6-8] As a consequence, the properties of other functional device can be modulated via controlling the resistance states of the memristor. Normally, such a modulation route could only be achieved in those hybrid systems which need to be externally connected each other. By contrast, embedding resistive switching layer into the single system does not need external connection, and thus makes it more readily to replace a circuit block of components in diverse applications.[9-11] Thus, developing new types of multifunctional devices integrating the memristor and other functions in the MIM structure itself is of great importance.

It is worth noting that a solid supercapacitor has the same device structure and materials choice as the memristor, which can store energy through the electrical polarization of dielectrics under an external voltage. Such a supercapacitor requires a

high breakdown voltage to induce more polarization charge. On the other hand, electroforming or set process is a soft breakdown to trigger the resistive switching, in which low operation voltages are beneficial to reduce the power consumption or enhance the sensitivity of memristive synapses.[12-15] Therefore, the two devices have been individually treated because of the competing relationship between polarization and resistive switching processes since the change of free charge determines the resistance state of the former while the latter is dominated by the polarization charge.[16] Recently, a capacitive-coupled memristive effect has been suggested to illustrate the non-pinched current–voltage (*I*-*V*) hysteresis loop based on a model of parallel connecting an ideal memristor and capacitor.[17] It also implies the feasible coexistence of the functions of the memristor and solid supercapacitor in principle.

As for dielectric capacitor, the energy storage density (J_{sto}) is too low to meet the requirement of advanced electronic and electrical systems although it has the highest power density in all energy storage devices.[18,19] Enhancing the breakdown strength (E_b) is considered to be the key to raise energy storage density due to $J_{sto} = \frac{1}{2}\varepsilon_0\varepsilon_r E_b^2$ for linear dielectrics, where ε_0 and ε_r are the permittivity of vacuum and the relative dielectric constant of the dielectrics, respectively.[20] Compared with the low breakdown fields (<1 MV cm^{-1}) in the bulk ceramics, the counterparts in the film form display huge applied fields (>3 MV cm^{-1}). Furthermore, the introduction of Al_2O_3 is a universal method to promote the breakdown strength of dielectrics because it possesses high dielectric strength and large band gap.[21-23] For example, the breakdown strength is enhanced by 80% in Al/$SrTiO_3$/Pt compared with that in

Au/$SrTiO_3$/Pt due to the formation of a new layer Al_2O_3 caused by anodic oxidation process.[22] Furthermore, a high energy density can reach up to 39.49 J cm^{-3} in $SrTiO_3$/anodized Al_2O_3 multilayer.[23] Similar strategy has also been deliberately designed to manipulate the resistive switching performance of the memristor. Natural aluminum oxide (AlO_x) layer can be self-formed at the Al/oxide interface because of its low standard Gibbs free energy of formation, which can act as an oxygen-reservoir to improve the stability and uniformity of switching characteristics.[24-26] Therefore, the existence of AlO_x layer between Al electrode and oxide insulator should play an important role in the operation of multifunctional MIM devices combining dielectric energy storage and resistive switching.

Ta_2O_5 has been widely employed as the insulator in the memristor and capacitor because of the existence of two thermodynamically stable phases in TaO_x and its relatively high dielectric constant of around 25 among binary oxides.[5,27-29] Its resistive switching characteristics show high dependence on the oxygen affinity of electrode materials associated with standard Gibbs energy of formation of oxides of the metals.[30,31] Different resistive switching behaviors can be found in TaO_{2-y}/Ta_2O_{5-x}/AlO_σ structure for the devices using Pt and Al top as electrodes, respectively.[31] In contrast to the electronic application of Ta_2O_5, few work has been devoted to its energy storage exploration.[32] In this work, we demonstrate Al/Ta_2O_5/Pt structure capable of simultaneously exhibiting both high energy storage density and ultralow current resistive switching. The Al/Ta_2O_5 interface effectively raises the breakdown voltage of the MIM structure, leading to a relatively high energy density.

Furthermore, resistance states can be tuned by the oxygen migration across the interface driven by applied voltage. The two functions co-existed in a same device structure make it more feasible for cooperative operation in an integrative way compared to those hybrid systems possessing energy storage and information process.

2. Results & Discussions

Figure 1(a) shows our design principle of energy storage in the MIM structure which requires a high breakdown voltage and a high dielectric polarization. One the contrary, a low HRS-LRS transition voltage and a high density of mobile species are generally expected in a memristor. In such a case, an abrupt resistance change can be usually observed due to the formation of conductive path. This is a so-called digital type resistive switching for resistive switching random access memory application because a large ratio of the resistance of HRS/LRS is expected to distinguish the two states of "0" and "1" easily, as shown in Figure 1(b). Another type switching is analog phenomenon displaying a gradual change of the device resistance, which can be used to mimic the potentiation/inhabitation of the synaptic weight.[33-35] The MIM device could remain highly insulative at the work mode of analog resistive switching. It indicates that dielectric energy storage and analog resistive switching can be implemented simultaneously in a same MIM device. To achieve the two functions, a bilayer structure is demonstrated in Figure 1(c). The TaO_x layer acts as a medium of polarization charge, and the Al/TaO_x interface is responsible for a large breakdown electric field. Furthermore, oxygen exchange between them and electrode layer

dominates the resistance change. Therefore, a bifunctional device with high energy storage density and ultralow current analog resistive switching is constructed, as shown in Figure 1(d).

Figure 2(a) presents cross-sectional SEM image of the Al/TaO_x/Pt device. The thickness of deposited TaO_x film was about 200 nm, which is very close to that measured by the profiler. No diffraction peak of TaO_x can be observed in the XRD pattern as shown in supplementary material Figure S1, revealing that the TaO_x film deposited at room temperature is amorphous. In addition, the AFM (supplementary material Figure S2) result shows the absence of obvious grain and very smooth surface, which is the typical morphology characteristic of amorphous films. The wide range survey XPS spectra with the increasing etching times (supplementary material Figure S3) also exhibit the transition from top Al electrode to TaO_x layer. Moreover, the measured peaks of Al 2*p* at the interface Al/TaO_x, and the Ta 4*f* at the TaO_x surface and at the inner TaO_x were carefully fitted to check the chemical states of the elements, as shown in Figures 2(b~d). The Al 2*p* signal can be attributed to the two contributions from the strong metallic and weak oxidation peaks, suggesting the formation of self-formed AlO_x at the interface. It is reasonable that the standard Gibbs free energy of formation of Al_2O_3 (−1582.9 kJ/mol (2/3 Al_2O_3) at 298 K) is much lower than that of Ta_2O_5 (−764.4 kJ/mol (2/5 Ta_2O_5) at 298 K). There are only two strong peaks of Ta $4f_{7/2}$ (26.12 eV) and Ta $4f_{5/2}$ (27.99 eV) for the TaO_x surface. A spin-orbit splitting of 1.87 eV and an area ratio of 0.79 between the components are obtained, suggesting a fully oxidized Ta_2O_5 state on the surface. But multiple states

can be found for the inner of the TaO_x film from the peaks of Ta $4f_{7/2}$ (26.68 eV, 24.88 eV, 23.8 eV, and 22.26 eV corresponding to Ta^{5+}, Ta^{3+}/ Ta^{4+}, Ta^{2+} and Ta^{1+}, respectively).[36] It implies the existence of sub-stoichiometric tantalum oxide in the film inner.

Figure 3(a) and Figure 3(b) compares the breakdown properties of Al/TaO_x/Pt and Au/TaO_x/Pt sandwich structures. Current density-electric field (*J-E*) curves suggest that dielectric breakdown characteristics of the TaO_x films are highly dependent on the top electrode employed in the MIM structure. The Au capped device shows a large current and a low breakdown strength of 2.33 MV cm^{-1}. The dielectric strength of Al capped device is enhanced to approximate 5 MV cm^{-1}. More than 50 devices have been measured, showing similar behavior as shown in supplementary material Fig. S4. It indicates high reliability of our developed devices. Moreover, its leakage current density is very low and remains stable about 7.6×10^{-7} A cm^{-2} until the ultimate breakdown. The effect of top electrodes on the breakdown strength and leakage suggests that the active metal like Al prefers to react with the oxide layer to form high insulative AlO_x. Particularly, further anodic oxidation process would happen when a positive voltage applied.[37] Therefore, the generated AlO_x at the Al/TaO_x interface improves the breakdown characteristics of device since it is a good insulator and possesses high breakdown strength. On the contrary, a relative low breakdown field is found under a negative voltage in the same Al/TaO_x/Pt structure due to the absence of anodic oxidation as shown in supplementary material Figure S5. Meanwhile, the process of breakdown was monitored by optical microscope. As

shown in the ultimate breakdown morphology in supplementary material Figure S6, only a few breakdown spots are observed on the Al surface, while widespread breakdown damage spots on the surface of Au electrode are found. It could be due to less Joule heating in the Al-capped device because of its lower power consumption with a lower leakage. The characteristic breakdown fields are further analyzed by Weibull distribution function:[38] $P(E) = 1 - \exp[-(E/E_b)^{\beta}]$, where *P(E)* is the cumulative probability of electric breakdown for a certain electric field, E_b is the Weibull characteristic of breakdown strength at which the cumulative probability is 63.21%, and β is the Weibull modulus denoting the dispersion of data. Figure 3(b) compares the characteristic breakdown strengths measured from the Au/TaO_x/Pt and Al/TaO_x/Pt. It is evident that E_b is greatly enhanced from 2.36 MV cm^{-1} of Au/TaO_x/Pt to 5.07 MV cm^{-1} of Al/TaO_x/Pt. The low and stable leakage as well as high breakdown strength make the Al/TaO_x/Pt device suitable to storage energy.

Figure 3(c) shows the dielectric constant and dielectric loss of Al/TaO_x/Pt as the functions of applied voltage at 3 MHz. Both of them remain stable while applying a voltage from 0 V to 20 V. The dielectric constant is 26.2 and dielectric loss is relatively low about 0.029. Thus, the maximum energy densities of Au/TaO_x/Pt and Al/TaO_x/Pt can be computed to be about 5.1 J cm^{-3} and 27.6 J cm^{-3}, respectively. Furthermore, energy storage densities of several types of binary oxide films with linear dielectric response are collected, as shown in Figure 3(d). Compared with the only one report about the energy storage of TaO_x film (14 J cm^{-3}),[32] the energy storage density of Al/TaO_x/Pt is almost doubled. Moreover, it is higher than the energy

storage density of Al/amorphous aluminium oxide (a-AO)/Pt (13.9 J cm^{-3}) which shows the similar mechanism and breakdown strength to this work when considering the dielectric constant of TaO_x is higher than that of a-AO.[39] Higher energy density was reported in the MIM structure of Al/Al_2O_3/ITO with a several-nm dielectric layer.[40] Since the breakdown strength relies on the dielectric thicknesses, the energy density would decrease to below 20 J cm^{-3} as the dielectric thickness exceeds 150 nm.

Figure 4(a) compares the current-voltage (*I-V*) hysteresis curves of Al/TaO_x/Pt and Au/TaO_x/Pt. A weak hysteresis with "figure-8" polarity is found in Au/TaO_x/Pt while "counter-figure-8" polarity is observed in Al/TaO_x/Pt, indicating that the Al electrode or the Al/TaO_x interface participates in the resistive switching process.[41] Opposite switching polarities have also been reported in (Pr, Ca)MnO_3 devices with active (Al) and inert (Pt) electrodes. The filaments based on oxygen ions diffusion under applied voltage dominates the transport properties of the Au capped device, which generally exhibits a typical "figure-8" switching characteristic. As mentioned above, the as-fabricated Al/TaO_x interface is consisted of Al, slightly oxidized AlO_x and TaO_x. When a positive voltage is applied, negative-charged oxygen ions in TaO_x layer would migrate to the Al top electrode. Due to the anode oxidation, the slightly AlO_x layer would be further oxidized and hence becomes thicker. As a result, the device would transform to a HRS rather than a LRS. Moreover, the operation current of Al/TaO_x/Pt memristor is very low about 1 nA, although the operation voltage is higher than 10 V.[42-45] Figure 4(b) compares the operation currents and powers of this work and other reported oxides-based memristors in which ultralow operation

currents have been emphasized. Our measured operation parameters are very close to those of Al_2O_3 memristor which exhibits the current lowest operation record among all oxide-based memristors.

In addition to the above *I-V* hysteresis behavior, multistate resistive switching is found in the device with a voltage sweep up to +12 V and −12V through continuous *I-V* cycling, as shown in Figures 4(c) and 4(d), respectively. The leakage of device shows a successive switching property that it decreases under positive bias voltage loop and increases under negative voltage loop, gradually. The tendency is agreement with the polarity of resistive switching curve in Figure 4(a). It is understandable that the oxygen content and thickness of the AlO_x interface can be modulated by the oxygen exchange between TaO_x and AlO_x and Al electrode driven by voltage bias. Furthermore, the current remains below 1 nA. It also indicates that analog resistive switching operates at ultralow operation current and energy storage is achieved with moderate energy density simultaneously.

Analog resistive switching properties are utilized to simulate the synaptic behaviors like short-term plasticity (STP) and long-term plasticity (LTP), as shown in Figure 5. The current of the device increases immediately when applying the pulse and decays to initial state spontaneously during the interval of pulses. Figure 5(a) shows such synchronous response to electric stimulus at -8 V pulse. Similar STP process is also observed at the initial stage of about a dozen pulses of -15 V (Figure 5(b)). Furthermore, the current is retained at the same level as that of the STP even after the removal of input pulse, revealing the transition from STP to LTP. In addition,

the current decay can well be fitted by the exponential decay law of biological excitatory synapses: $I = I_0 + Aexp(-t/\tau)$, where A is a constant, τ is the time constant, and t is the time after applying each input pulse. As shown in Figure 5(c), τ increases gradually under the successive pulse stimulus. It indicates that the history of oxygen exchange between the interfaces of Al/AlO_x and AlO_x/TaO_x can be maintained after every pulse. Meanwhile, paired-pulse facilitation (PPF) is a physiological phenomenon associated with STP. A net increase in the synaptic response will occur when two identical stimulus arrive in rapid succession. PPF index model is expressed as: $PPF = \frac{I_2 - I_1}{I_1} \times 100\%$, where I_1 and I_2 correspond to the current of first and second pulse, respectively.[13] Fitting of the PPF curves shows that the device plasticity decays exponentially vs. inter-pulse time interval, as shown in Figure 5(d). Therefore, the results suggest that our fabricated device can be used as not only energy device but also memristive device. Different from the previous hybrid systems externally connecting energy storage units and a memristor, the MIM structure in this work can implement the two functions via the interface layer effect by itself in a single system. Therefore, the coupling between the so-called competed properties is appealing in the MIM structure. The availability of the bifunctional device make it more feasible for cooperative operation in an integrative way compared to those hybrid systems. Moreover, resistive states can be controlled not only by ions transport, but also by electron, photo, magnetism, pressure, or temperature.[46] It also indicates extra degrees of freedom for creating novel energy storage and memristive multifunctional devices in a MIM structure exhibiting those resistive switching mechanisms.

3. Conclusions

In summary, we developed a bifunctional device of simple and commonly used Al/TaO_x/Pt exhibiting energy storage and memristive properties simultaneously. The breakdown measurement and resistive switching polarities of Al/TaO_x/Pt and Au/TaO_x/Pt reveal the crucial role of AlO_x layer at the Al/TaO_x interface. Energy density of Al/TaO_x/Pt reaches to 27.6 J cm^{-3} at 5.07 MV cm^{-1}. Meanwhile, synaptic behaviors like STP and LTP are realized based analog resistive switching with ultralow operating current of sub-nanoampere. Such a bifunctional device might enhance the flexibility of integration of electronic and energy devices, provide an opportunity of coupling between different functions, and promote diverse applications of such structure device in modern functional electronics.

4. Experimental

TaO_x thin films were fabricated on cleaned commercial Pt/Si substrates at room temperature using a tantalum target (99.99% purity, 2 in. in diameter) by direct current reactive magnetron sputtering. During film deposition, the working gas pressure was 0.45 Pa with argon/oxygen ratio of 1:1 and the sputtering power was 107 W. Two top metal electrodes, Al and Au, were then prepared on TaO_x films through a shadow mask to form circle spots (200 μm in diameter). Film thickness was confirmed by profiler (Dektak-XT, Bruker) and field-emission scanning electron microscope (FESEM, Ultra55, Carl zeiss NTS GmbH). The crystallinity was

characterized by X-ray diffraction (XRD, Philips X'pert MPD Pro) using Cu Kα radiation. Surface morphology of the thin film was examined by atomic force microscope (AFM, SPA-300HV). Moreover, the chemical states of the elements in the films were investigated by X-ray photoelectron spectrometer (XPS, Thermo Fisher Scientific K-Alpha). Electrical characteristics were studied by Keithley 2400 SourceMeter and Keithley 4200A-SCS. After electrical measurement, the surface morphology of top electrodes was examined by optical microscope (BX051 Olympus).

Supporting information

Supporting information is available from the Wiley Online Library or from the author.

Acknowledgements

This work was supported by the National Natural Science Foundation of China (51772252), the Sichuan Science and Technology Program (2020JDRC0062), and the Project of State Key Laboratory of Environment-friendly Energy Materials, Southwest University of Science and Technology (18FKSY0202, 19FKSY09).

Conflict of interest

The authors declare no conflict of interest.

References

[1] L. O. Chua, *IEEE Trans. Circuit Theory* **1971**, *18*, 507.

[2] D. B. Strukov, G. S. Snider, D. R. Stewart, and R. S. Williams, *Nature* **2008**, *453*, 80.

[3] M. A. Zidan, J. Paul Strachan, and W. D. Lu, *Nature Electronics* **2018**, *1*, 22.

[4] F. Pan, S. Gao, C. Chen, C. Song, and F. Zeng, *Mater. Sci. Eng. R* **2014**, *8*, 31.

[5] J. J. Yang, D. B. Strukov, and D. R. Stewart, *Nature Nanotech.* **2013**, *8*, 13.

[6] B. Liu, B. Y. Liu, X. F. Wang, X. H. Wu, W. N. Zhao, Z. M. Xu, D. Chen, and G. Z. Shen, *Adv. Mater.* **2014**, *26*, 4999.

[7] M. Qi, X. Zhang, L. Yang, Z. Q. Wang, H. Y. Xu, W. Z. Liu, X. N. Zhao, and Y. C. Liu, *Appl. Phys. Lett.* **2018**, *113*, 223503.

[8] X. Yang, C. X. Shan, Q. Liu, M. M. Jiang, Y. J. Lu, X. H. Xie, B. H. Li, and D. Z. Shen, *ACS Photonics* **2018**, *5*, 1006.

[9] J. L. Zhao, K. L. Teo, K. Zheng, and X. W. Sun, *Nanotechnology* **2016**, *27* 115204.

[10] Y. R. Park, W. K. Choi, and Y. J. Hong, Curr. *Appl. Phys.* **2019**, *19*, 102.

[11] K. Hong, M. G. Kim, H. M. Yang, D. C. Lim, J. Y. Lee, S. J. Kim, I. Lee, K. H. Lee, and J. L. Lee, *Adv. Energy Mater.* **2016**, *6*, 1600651.

[12] S. Li, H. Z. Zeng, S. Y. Zhang, and X. H. Wei, *Appl. Phys. Lett.* **2013**, *102*, 153506.

[13] L. Hu, S. Fu, Y. Chen, H. Cao, L. Liang, H. L. Zhang, J. H. Gao, J. R. Wang, and F. Zhuge, *Adv. Mater.* **2017**, *29*, 1606927.

[14] Y. C. Wang, L. Hu, X. H. Wei, and F. Zhuge, *Appl. Phys. Lett.* **2020**, *116*, 221602.

[15] Y. Yang, H. Y. Du, Q. Xue, X. H. Wei, Z. B, Yang, C. G. Xu, D. M. Lin, W. J. Jie, and J. H. Hao, *Nano Energy* **2019**, *57*, 566.

[16] A. Molinari, R. Witte, K. K. Neelisetty, S. Gorji, C. Kübel, I. Münch, F. Wöhler, L. Hahn, S. Hengsbach, K. Bade, H. Hahn, and R. Kruk, *Adv. Mater.* **2020**, *32*, 1907541.

[17] B. Sun, Y. Z. Chen, M. Xiao, G. D. Zhou, S. Ranjan, W. T. Hou, X. L. Zhu, Y. Zhao, S. A.T. Redfern, and Y. N. Zhou, *Nano Lett.* **2019**, *19*, 6461.

[18] H. Pan, F. Li, Y. Liu, Q. H. Zhang, M. Wang, S. Lan, Y. P. Zheng, J. Ma, L. Gu, Y. Shen, P. Yu, S. J. Zhang, L. Q. Chen, Y. H. Lin, and C. W. Nan, *Science* **2019**, *365*, 578.

[19] X. H. Hao, *J. Adv. Dielect.* **2013**, *3*, 1330001.

[20] Y. B. Wang, W. J. Jie, C. Yang, X. H. Wei, and J. H. Hao, *Adv. Funct. Mater.* **2019**, *29*, 1808118.

[21] T. D. Zhang, W. L. Li, Y. Zhao, Y. Yu, and W. D. Fei, *Adv. Funct. Mater.* **2018**, *28*, 1706211.

[22] W. B. Gao, M. W. Yao, and X. Yao, *Ceram. Int.* **2017**, *43*, 13069.

[23] W. B. Gao, M. W. Yao, and X. Yao, *ACS Appl. Mater. Interfaces* **2018**, *10*, 28745.

[24] K. K. Chiang, J. S. Chen, and J. J. Wu, *ACS Appl. Mater. Interfaces* **2012**, *4*, 4237.

[25] H. F. Ling, M. D. Yi, M. Nagai, L. H. Xie, L. Y. Wang, B. Hu, and W. Huang, *Adv. Mater.* **2017**, *29*, 1701333.

[26] Q. H. Li, L. J. Qiu, X. H. Wei, B. Dai, and H. Z. Zeng, *Sci. Rep.* **2016**, *6*, 29347.

[27] H. Matsuhashi, and S. Nishikawa, *Jpn. J. Appl. Phys.* **1994**, *33*, 1293.

[28] M. J. Lee, C. B. Lee, D. Lee, S. R. Lee, M. Chang, J. H. Hur, Y. B. Kim, C. J. Kim, D. H. Seo, S. Seo, U. I. Chung, I. K. Yoo, and K. Kim, *Nature Mater.* **2011**, *10*, 625.

[29] K. M. Kim, S. R. Lee, S. Kim, M. Chang, and C. S. Hwang, *Adv. Funct. Mater.* **2015**, *25*, 1527.

[30] C. Chen, S. Gao, F. Zeng, G. S. Tang, S. Z. Li, C. Song, H. D. Fu, and F. Pan, *J. Appl. Phys.* **2013**, *114*, 014502.

[31] X. Y. Li, H. Q. Wu, B. Gao, W. Wu, D. Wu, N. Deng, J. Cai, and H. Qian, *Nanotechnology* **2016**, *27*, 305201.

[32] G. Sethi, M. Olszta, J. Li, J. Sloppy, M. W. Horn, E. C. Dickey, and M. T. Lanagan, *2007 Annual Report Conference on Electrical Insulation and Dielectric Phenomena*, **2007**, *815*.

[33] Y. Lin, C. Wang, Y. Y. Ren, Z. Q. Wang, H. Y. Xu, X. N. Zhao, J. G. Ma, and Y. C. Liu, *Small Methods* **2019**, *3*, 1900160.

[34] S. Kim, H. Kim, S. Hwang, M. H. Kim, Y. F. Chang, and B. G. Park, *ACS Appl. Mater. Interfaces* **2017**, *9*, 40420.

[35] X. B. Yin, R. Yang, K. H. Xue, Z. H. Tan, X. D. Zhang, X. S. Miao, and X. Guo, *Phys. Chem. Chem. Phys.* **2016**, *18*, 31796.

[36] S. Kasatikov, E. Filatova, S. Sakhonenkov, A. Konashuk, and A. Makarova, *J. Phys. Chem. C* **2019**, *123*, 6849.

[37] M. X. Li, M.W. Yao, Z. Su, W. B. Gao, and X. Yao, *Ceram. Int.* **2018**, *44*, 21428.

[38] L.Yang, X. Kong, F. Li, H. Hao, Z. Cheng, H. Liu, J. F. Li, and S. Zhang, *Prog.*

Mater. Sci. **2019**, *102*, 72108.

[39] Z. Su, M. W. Yao, M. X. Li, W. B.Gao, Q. X. Li, Q. Feng, and X. Yao, *J. Phys. Chem. C* **2018**, *6*, 5616.

[40] H. Spahr, C. Nowak, F. Hirschberg, J. Reinker, W. Kowalsky, D. Hente, and H. H. Johannes, *Appl. Phys. Lett.* **2013**, *103*, 042907.

[41] S. L. Li, Z. L. Liao, J. Li, J. L. Gang, and D. N. Zheng, *J. Phys. D: Appl. Phys.* **2009**, *42*, 045411.

[42] Y. Wu, B. Lee, and H. S. P. Wong, *IEEE Electr. Device L.* **2012**, *31*, 12.

[43] S. G, F. Cai, J. Zhou, and W. D. Lu, *IEEE Electr. Device L.* **2014**, *35*, 12.

[44] K. Z, K. Sun, F. Wang, Y. Han, Z. Jiang, J. Zhao, B. Wang, H. Zhang, X. Jian, and H. S. Philip Wong, *IEEE Electr. Device L.* **2015**, *36*, 10.

[45] Y. S. Chen, H. Y. Lee, P. S. Chen, W. S. Chen, K. H. Tsai, P. Y. Gu, T. Y. Wu, C. H. Tsai, S. Z. Rahaman, Y. D. Lin, F. Chen, M. J. Tsai, and T. K. Ku, *IEEE Electr. Device L.* **2013**, *35*, 2.

[46] X. Pan, T. Jin, J. Gao, C. Han, Y. Shi, and W. Chen, *Small* **2020**, *16*, 2001504.

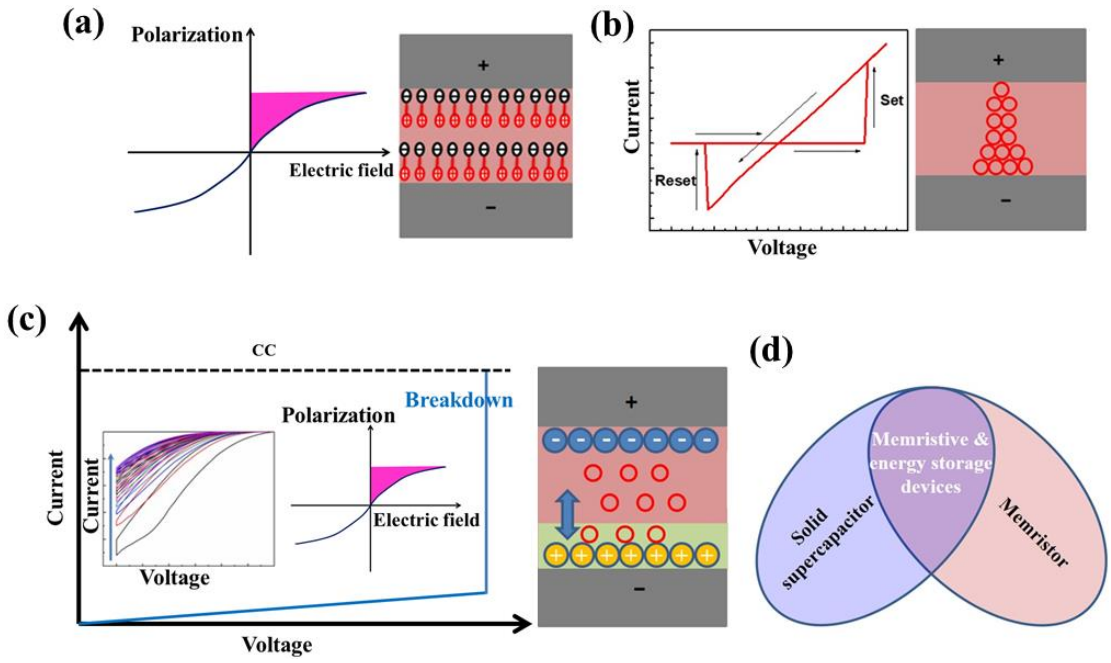

Figuer 1. The operation principle of devices: (a) dielectric capacitor for energy storage, the shadowed area represents the energy density; (b) memristor for digital resistive switching; (c) bifunctional device for energy storage and memristive properties; (d) coexistence of the memristor and solid supercapacitor.

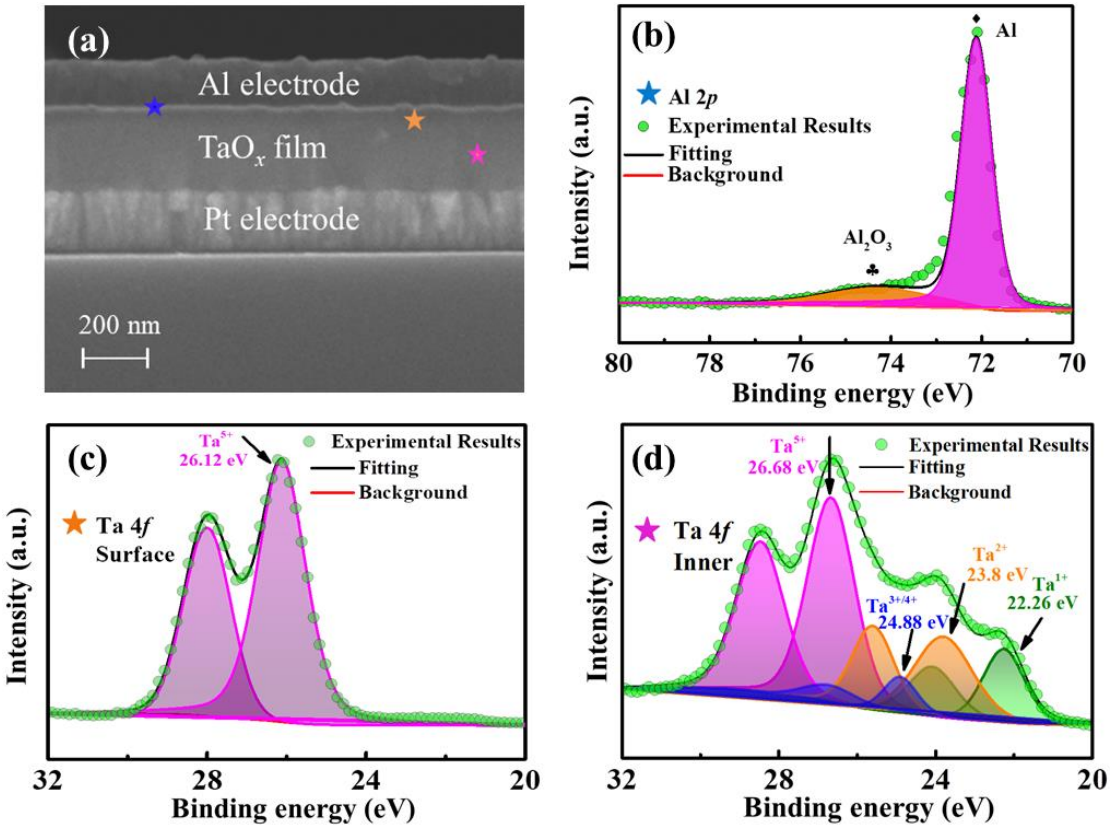

Figure 2. (a) Cross-sectional FESEM image of Al/TaO$_x$/Pt; (b) Al 2p XPS spectra at the interface; (c) - (d) Ta 4*f* XPS spectra of TaO$_x$ film: surface and inner.

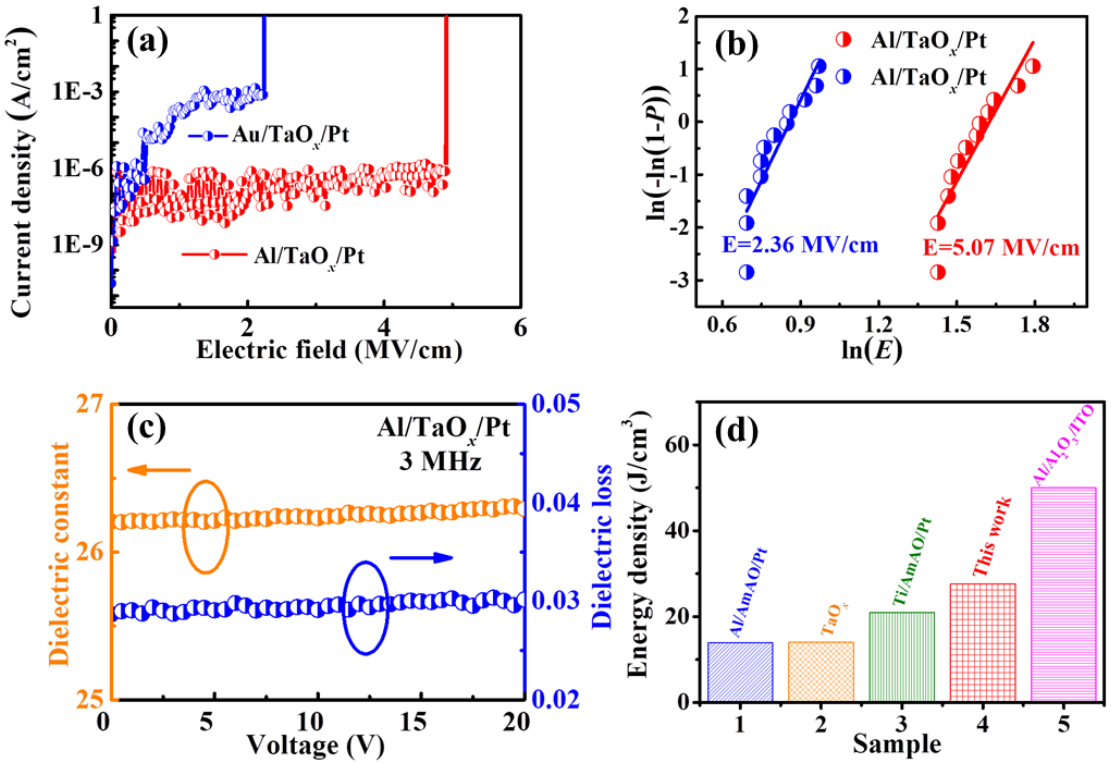

Figure 3. Dielectric properties of devices: (a) *J-E* characteristic; (b) Weibull distribution of dielectric breakdown strength; (c) dielectric constant and dielectric loss as the function of applied voltage; (d) comparison of energy densities of different binary oxide films with linear dielectric response.

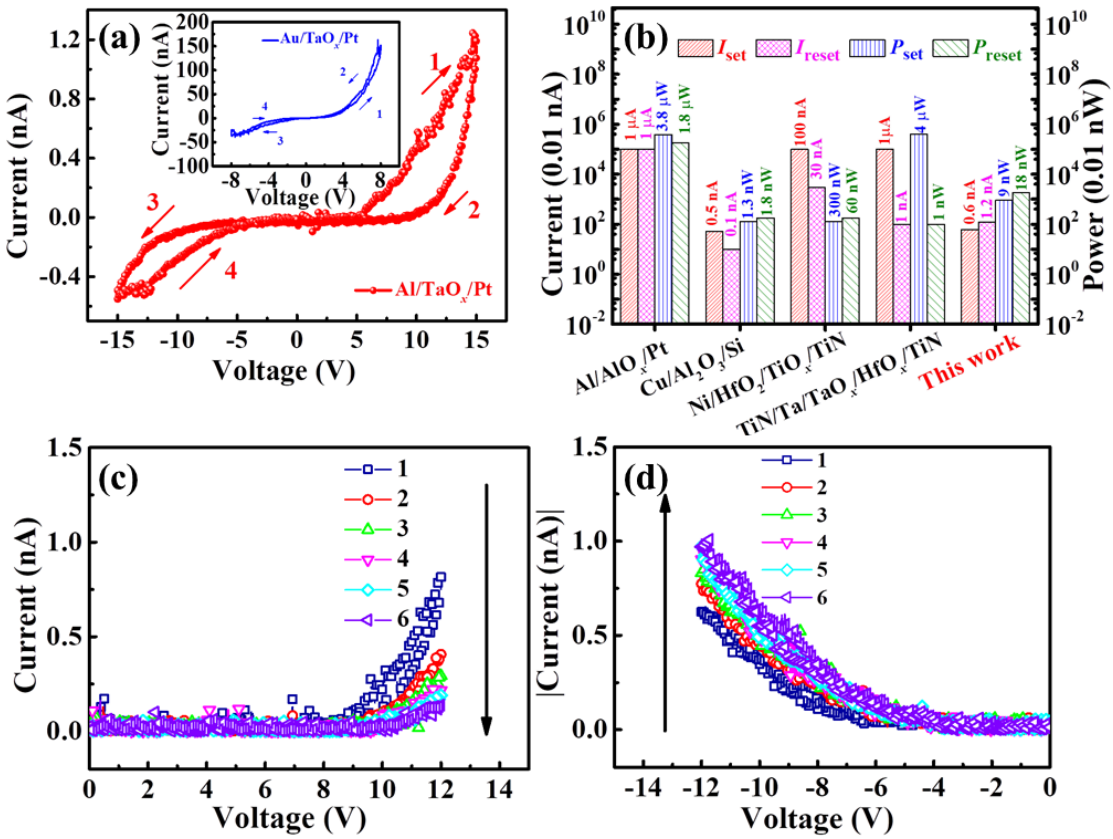

Figure 4. Resistive switching characteristics of Al/TaO$_x$/Pt: (a) typical *I-V* switching curve, inset shows *I-V* characteristic of Au/TaO$_x$/Pt; (b) comparison of the switching performance metrics between this work and previous reports with ultralow operation currents; (c) and (d) successive *I-V* switching curves from 0 to 12 V and 0 to −12 V, respectively.

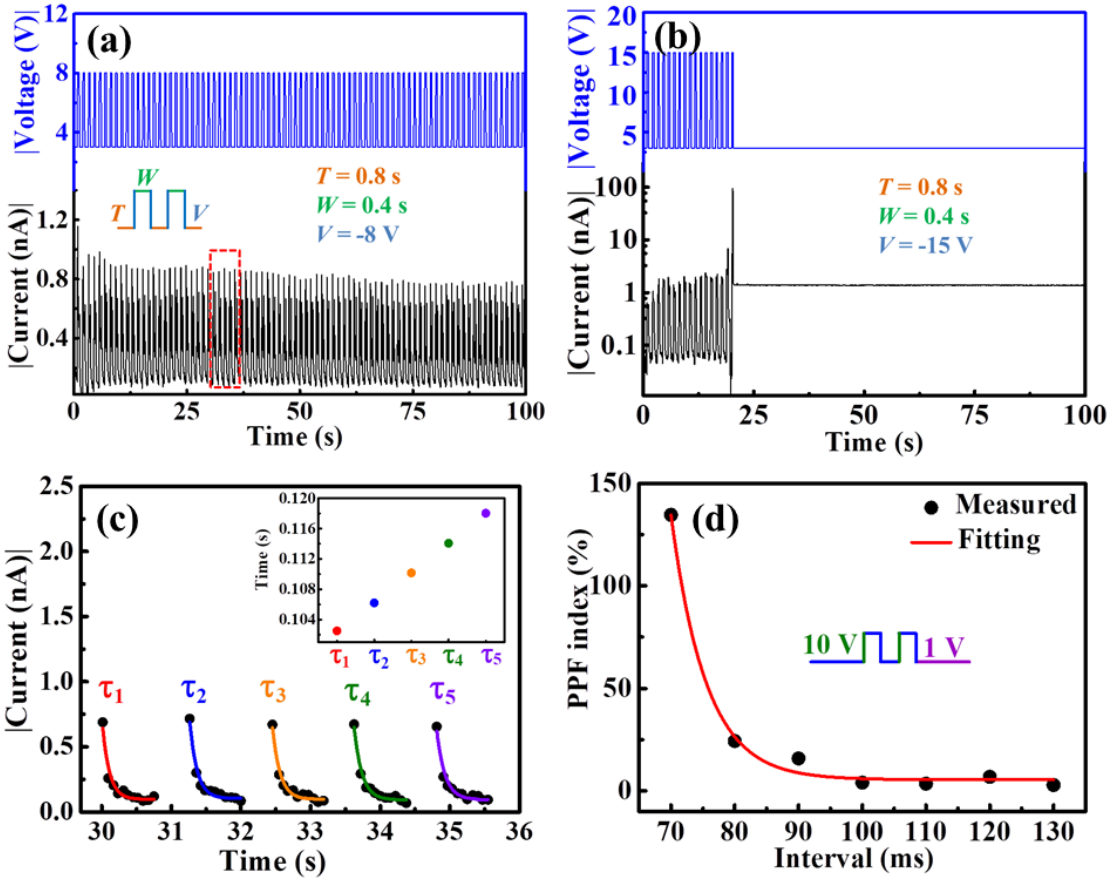

Figure 5. Synaptic behaviors of Al/TaO_x/Pt: (a) STP, W = 400 ms, V = -8 V, T = 0.8 s; (b) LTP, W = 400 ms, V = -15 V, T = 0.8 s; (c) the fitting result of conductance decay in (a) marked dotted rectangle; (d) pulse interval dependence of the PPF index.

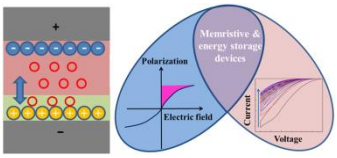

ToC figure.

ToC text: A bifunctional device capable of simultaneously achieving dielectric energy storage and resistive switching is proposed based on a conventional metal-insulator-metal structure. Both of the device properties are found to be correlated to the role of AlO_x interfacial layer between Al electrode and the dielectric layer.